OPEN ACCESS

FAULT DETECTION AND DIAGNOSIS OF HIGH-VOLTAGE LOAD SYSTEM FOR ELECTRIC HEAVY TRUCK (EHT) BASED ON RESPONSE SIGNAL ANALYSIS

Jinfeng Zheng[1], Yuan Zhang[1], Yanbo Hui[1]*, Bo Chen[2], Haiyang Ding[3]*
Qiao Wang[2], Xianglong You[4], Xiaoxuan He[2], Yifei Zhang[2]
[1]College of Electromechanical Engineering, Henan University of Technology, Zhengzhou, 450001, China
[2]College of Electrical Engineering, Henan University of Technology, Zhengzhou, 450001, China
[3]Weihua Group Co., LTD., Changyuan, 453400, China
[4]College of Automobile and Traffic Engineering, Nanjing Forestry University, Nanjing, 210037, China

Abstract - This paper proposes a system-level fault diagnosis scheme applicable to the high-voltage load system of electric heavy truck (EHT). Firstly, when the vehicle is offline, the main current response signal of the high-voltage load system of the electric heavy truck is obtained by using a current sensor and a data acquisition system. The time-domain characteristics of the response signals extracted under normal system conditions are used to construct the health baseline. Then, the Mahalanobis distance between the characteristics of the signal to be measured and the health baseline is calculated as the fault detection index. Furthermore, novel geometric features were extracted from the response signal. These features consist of the number of frame lines, pulse height, effective value, transition time, and equivalent pulse width. Additionally, the above features extracted from the geometric feature vector samples were utilised to construct a dictionary matrix, and the batch matching tracking method was adopted to calculate the sparse vectors of all test samples. Finally, the mode of the test sample is determined through local zeroing and reconstruction error to achieve fault diagnosis. For the proposed method, the fault diagnosis results of all test samples were consistent with the expected results, which proved the effectiveness of the fault diagnosis method proposed in this study.

Keywords: Electric heavy truck (EHT), Fault diagnosis, Geometric feature extraction, Sparse representation, High-voltage load system.

1. Introduction

With the growing global emphasis on environmental protection, carbon emissions in the transportation sector have attracted increasing attention [1]. In an effort to mitigate the energy crisis and reduce environmental pollution, electric heavy trucks (EHTs) have been progressively replacing traditional fuel-powered heavy-duty vehicles in recent years [2]. Unlike their fuel-powered counterparts, the high-voltage load system, serving as the core component of EHTs, poses a significant risk to operational safety and efficiency when faults occur—such failures can lead to reduced power output and a markedly increased risk of vehicle downtime. Consequently, fault detection and diagnosis of high-voltage load systems have become both a pressing need and a key direction for future development [3]. Given the greater complexity of high-voltage load systems in EHTs compared to conventional fuel-based trucks, system-level fault diagnosis offers more practical value than the diagnosis of individual components.

To diagnose faults in the high-voltage load system of electric heavy truck in a timely manner, scholars' research has mainly focused on diagnosing single components of electric truck, including power converters [4], charging devices [5], drive motors [6 7], air conditioning busbar capacitors [8], etc. For example, fault diagnosis methods for power converters include online fault diagnosis with feature fusion, sensitive feature extraction, and genetic algorithms [9]. Convolutional neural networks and signal analysis methods are used to diagnose faults in drive motors [10], and online capacitance estimation techniques are used to

https://doi.org/10.17683/ijomam/issue22.v1.1

diagnose faults in air conditioning busbar capacitors [11].

However, these methods are not applicable to system-level fault diagnosis in electric heavy trucks (EHTs), because a fault in a single component within the EHT high-voltage load system can also affect the overall operational status of the truck. Conducting fault diagnosis on the high-voltage load system as a whole can significantly improve the efficiency of fault detection. The EHT high-voltage load system can be considered as a small-scale microgrid. By investigating fault detection and diagnosis methods used in microgrids, it is found that Impulse Frequency Response Analysis (IFRA) is commonly applied in the performance evaluation of microgrid fault diagnosis [12]. Methods for assessing the health status of electrical equipment mainly fall into three categories: health index-based methods, machine learning-based methods, and uncertainty reasoning-based methods. Machine learning-based approaches require a large amount of sample data, such as Support Vector Machines [13], Adaptive Neuro-Fuzzy Inference Systems [14], and Fuzzy C-Means Clustering [15]. Uncertainty reasoning-based methods, including fuzzy inference [16], evidence theory [17], and multi-layered architectures [18], are unable to accurately reflect the relationships between different features.

A pulse signal, acting as the excitation input of the system, is injected to induce system responses, which can then be captured by sensors and analysed in the time domain, frequency domain, or time–frequency domain [19]. Techniques such as Impulse Response Analysis (IRA) have proven highly effective in identifying potential faults such as partial discharges within transformers, offering early warnings for equipment in operation [20]. The effectiveness of frequency-domain methods has also been validated through partial discharge simulations in winding models [21]. Time-domain analysis methods, which extract signal features such as peak value, root mean square (RMS), and maximum amplitude, are commonly employed to identify simple fault patterns [22].

Although IRA-based methods have been widely applied in fault detection and diagnosis within power systems, they are not fully applicable to the high-voltage load system of electric heavy trucks (EHTs) studied in this work. The high-voltage load system in EHTs consists of capacitive, resistive, and inductive loads, which differ significantly from the load structures typically found in conventional power systems. As a result, relying solely on a single response signal makes it difficult to accurately identify various fault types. Furthermore, the excitation signal in EHTs is generated through the on–off switching of relays controlled by the battery pack system, making it challenging to obtain standard pulse voltage signals in such systems. Therefore, in order to achieve effective fault diagnosis using the IRA method within EHT high-voltage load systems, improvements are required in both the generation of impulse signals and the acquisition and analysis of system response signals.

Therefore, in this study, we propose a system-level fault diagnosis scheme for the high-voltage load system of electric heavy trucks (EHTs), based on an improved Impulse Response Analysis (IRA) method. In this scheme, the mainline current response signal is collected using a current sensor, segmented into frames, and analysed by extracting time-domain features. Faults are detected by calculating and normalising the Mahalanobis distance. An adaptive framing strategy based on a pulse-matching sliding-window drop method is employed to extract geometric features, which are then used to construct feature vectors and a dictionary matrix. Finally, sparse representation-based classification is applied to identify specific fault types.

The primary contributions of this paper are as follows:

For the high-voltage load system of electric heavy truck, a system-level, rapid fault detection and diagnosis approach is proposed, based on the impulse response analysis method, which requires only the acquisition of the main line current response signal.

To address the requirement for rapid fault detection in high-voltage load systems of electric heavy-duty trucks, a Mahalanobis distance-based fault detection metric calculation method is developed, which exclusively utilises impulse response signal sample sets obtained under fault-free conditions.

To fulfil the fast fault diagnosis demand of EHT high-voltage load systems, a unified geometric feature extraction technique is proposed, based on pulse-matching signal framing, which significantly enhances the efficiency of geometric feature extraction.

2. Fault Detection and Diagnosis Method

In response to the operational requirements for fault detection and diagnosis in the high-voltage load system of electric heavy truck, this study employs the EHT battery pack system as the power source. By controlling the switching of relays, standard impulse signals are generated. Meanwhile, current sensors and a data acquisition system are used to collect the corresponding impulse response signals. Through analysis of these impulse response signals, fault detection and diagnosis of the high-voltage load system in electric heavy trucks can be achieved, as illustrated in Figure 1.

Both fault detection and fault diagnosis are carried out based on the analysis of impulse response signals. Fault detection mainly includes time-domain feature extraction, Mahalanobis distance calculation, and fault index computation; fault diagnosis mainly comprises pulse matching framing, geometric feature extraction, and sparse representation-based classification.

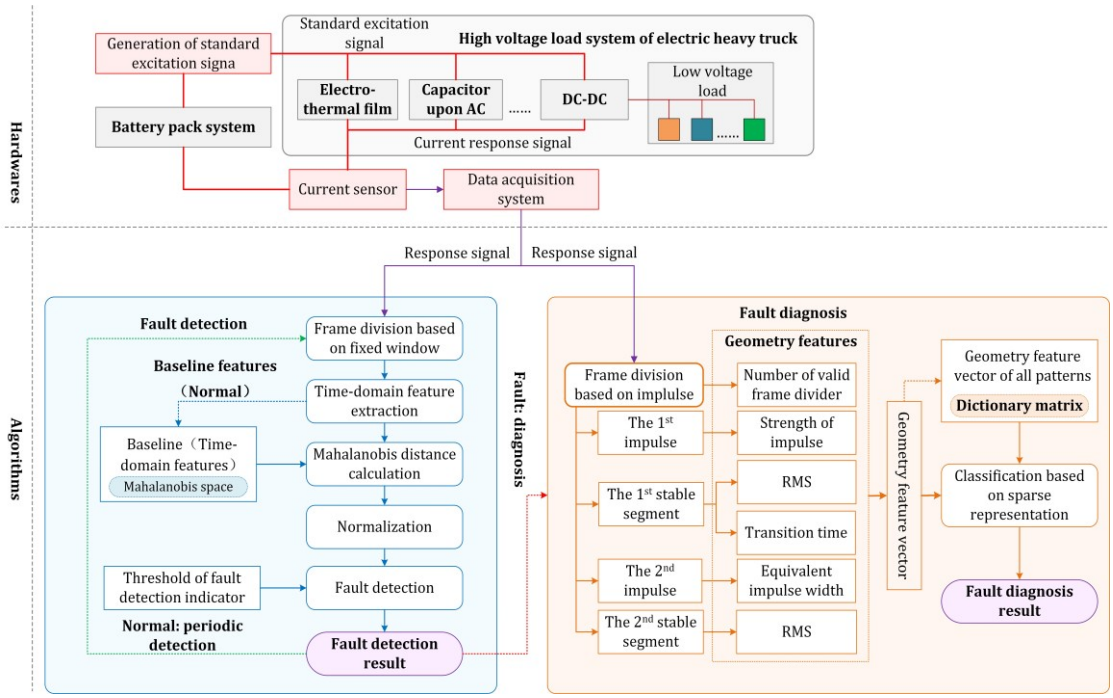

Figure 1: Fault detection and fault diagnosis of high voltage load system

2.1. Engineering Background and Hardware System

2.1.1 Introduction to the High-Voltage Load System of electric Heavy Truck

The high-voltage load system of electric heavy trucks (EHTs) is directly connected to the battery pack system and serves as a critical component in ensuring normal vehicle operation. It primarily comprises the traction motor, battery heating film, air-conditioning bus capacitor, and DC-DC module. Among these, the traction motor provides power for the EHT and, as a core component, is characterized by high reliability and a low failure rate. The battery heating film is used to heat the battery pack under low-temperature conditions; however, due to prolonged exposure to high temperatures and potential detachment from the battery casing, it is prone to wear and frequently suffers from local open-circuit faults. The air-conditioning bus capacitor is a key component for powering the air-conditioning system and is susceptible to performance degradation after extended service life due to component ageing. The DC-DC module, typically an isolated device, converts the high-voltage direct current supplied by the battery pack into low-voltage direct current. It is often affected by chassis vibrations, which can lead to coil disconnection or intermittent connections.

Faults in any of these critical components may affect the output of the battery pack, the operation of the vehicle's air-conditioning system, and the normal functioning of both the battery management system and the vehicle control system, ultimately compromising overall vehicle performance. Therefore, timely fault detection and diagnosis of the high-voltage load system, followed by appropriate maintenance actions based on diagnostic results, can effectively ensure the safe operation of EHTs, enhance maintenance efficiency, and improve overall vehicle economy.

2.1.2 Standard Impulse Signal Generation and Response Signal Acquisition

Considering the ease of engineering implementation for fault detection and diagnosis, this study draws inspiration from techniques used in the diagnosis of high-voltage load systems in electric buses [19]. The standard impulse voltage signal employed in this study is defined by the output voltage of the battery pack, and its waveform takes the form of a step signal, which can be generated through the opening and closing of a relay.

This method of impulse signal generation is straightforward and easy to implement, as illustrated in Figure 2. The resultant standard impulse signal is as follows:

$$u=\begin{cases}0,\ t\in[0,t_1)\text{s}\\ U,\ t\in[t_1,t_2)\text{s}\\ 0,\ t\in[t_2,t_3]\text{s}\end{cases} \tag{1}$$

Where U denotes the output voltage of the battery pack system.

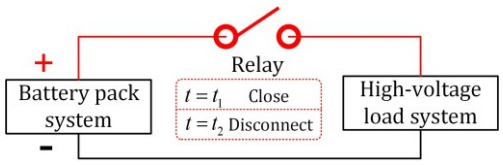

Figure 2: Standard impulse signal acquisition method

In the offline state of the vehicle, the main circuit current response signal of the high-voltage load system in the electric heavy truck is acquired using current sensors and a data acquisition system. This current signal encompasses the total current response signal of the battery heating film, the air-conditioning bus capacitor, and the DC-DC converter.

2.2 Fault Detection Method

In this section, time-domain features extracted from impulse response signals under normal system conditions are used to construct a health baseline. The same time-domain features are then extracted from the signal under inspection. Subsequently, the Mahalanobis distance between the features of the test signal and the health baseline is calculated and normalised to serve as the fault detection index. This method requires only normal (fault-free) samples, making it highly practical for engineering applications. Given the frequent execution of the fault detection algorithm, non-overlapping framing with a relatively large window width is employed, thereby effectively reducing the computational burden associated with fault detection.

2.2.1 Response Signal Framing and Time-Domain Feature Extraction

Assuming that the response signal $\boldsymbol{S_R}$ has a duration oft seconds, and that the signal is sampled at a rate of f_S samples per second, then the total number of samples, denoted by n_R, is given by:

$$n_R = f_s \cdot t_3 \tag{2}$$

Define the window width as w_1, that is, each window contains w_1 signal points. Non-overlapping windows are used for frame division, meaning that there is no overlap between the $i-1$ th frame and the i th frame. Then, the number of signal frames n_1 is:

$$n_1 = \text{floor}\left(n_R / w_1\right) \tag{3}$$

Among them, floor () is the function for rounding down.

Assuming that the i -th frame is denoted as $\boldsymbol{F_i}$, Its effective value and maximum value are denoted as $F_{i,\text{RMS}}$ $\boldsymbol{F_1}$ and $F_{i,\max}$ respectively, then the time-domain feature vector $\boldsymbol{F_T}$ extracted from the response signal $\boldsymbol{S_R}$ is:

$$\boldsymbol{F_T}=\left(F_{1,\text{RMS}}\quad F_{2,\text{RMS}}\quad\cdots\quad F_{n_1,\text{RMS}}\quad F_{1,\max}\quad F_{2,\max}\quad\cdots\quad F_{n_1,\max}\right)^T \tag{4}$$

The size of the time-domain feature vector $\boldsymbol{F_T}$ is: $2n_1\times 1$.

2.2.2 Health Baseline Construction and Mahalanobis Distance Calculation

Mahalanobis distance is used to define the statistical distance between a single sample and a sample population. Since Mahalanobis distance takes into account the correlation between signal features and is scale-invariant, it can enhance the effectiveness of fault detection. In this section, the health baseline is constructed using time-domain feature vectors obtained under normal system conditions. Assuming that the j -th time-domain feature vector used to construct the health baseline is denoted as $\boldsymbol{F_{T,Tr,j}}$, and the total number of samples is n_{Tr}, the health baseline $\boldsymbol{M_{Tr}}$ can be expressed as:

$$\boldsymbol{M_{Tr}}=\left(\boldsymbol{F_{T,Tr,1}}\quad\boldsymbol{F_{T,Tr,2}}\quad\cdots\quad\boldsymbol{F_{T,Tr,j}}\quad\cdots\quad\boldsymbol{F_{T,Tr,n_{Tr}}}\right) \tag{5}$$

The size of the health baseline $\boldsymbol{M_{Tr}}$ is $2n_1\times n_{Tr}$.

Assuming that the time-domain feature vector extracted from the test sample is denoted as $\boldsymbol{F_{T,Te}}$, the corresponding Mahalanobis distance is calculated as:

$$d_M\left(\boldsymbol{F_{T,Te}}\right)=\sqrt{\left(\boldsymbol{F_{T,Te}}-\overline{\boldsymbol{M_{Tr}}}\right)^T\boldsymbol{\Sigma}^{-1}\left(\boldsymbol{F_{T,Te}}-\overline{\boldsymbol{M_{Tr}}}\right)^T} \tag{6}$$

Where $d_M\left(\boldsymbol{F_{T,Te}}\right)$ denotes the Mahalanobis distance between the test sample vector and the health baseline matrix, $\overline{\boldsymbol{M_{Tr}}}$ represents the mean vector of the health baseline matrix, and $\boldsymbol{\Sigma}$ is the covariance matrix of the health baseline matrix.

2.2.3 Mahalanobis Distance Normalisation and Fault Detection

Due to the relatively large scale of the Mahalanobis distance, a normalisation function is applied in this section to narrow its range and facilitate fault detection. and then the influence of

dimensional units and inter-feature correlations is eliminated, thereby enhancing the comparability and stability of the distance measurement. Moreover, this normalisation improves robustness to noise and outliers in the data, preventing certain dimensions from exerting a disproportionate influence on the overall distance, thus making the method more suitable for fault detection tasks.

This study normalises the Mahalanobis distance using the arctangent function to obtain the fault detection index, as shown in Equation (7):

$$FDI = \left(\arctan d_M\left(\boldsymbol{F}_{T,Te}\right) - \arctan\alpha\right) \Big/ \left(\pi/2 - \arctan\alpha\right) \quad (7)$$

Where FDI denotes the fault detection index, and α represents the normalisation factor.

2.3 Fault Diagnosis Method

In this study, system-level fault diagnosis of the high-voltage load system is achieved through the analysis of response signals. To provide a more intuitive illustration of the signal framing process, Figure 3 presents the original signal under the normal operating condition, processed using a non-overlapping sliding window framing method. Each frame has a length of 3,000 sampling points, resulting in a total of 30 frames. The frame boundaries are indicated in the figure by red dashed lines.

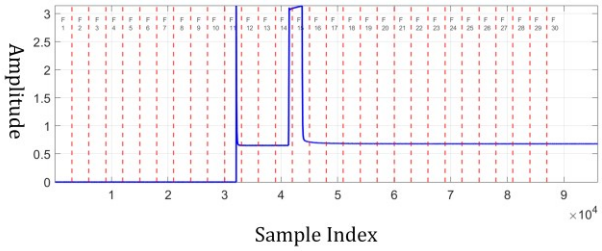

Figure 3: Real signal with frame annotations

To facilitate the definition of various segments within the response signal, this section uses the response signal under normal system operating conditions as an example, as illustrated in Figure 4.

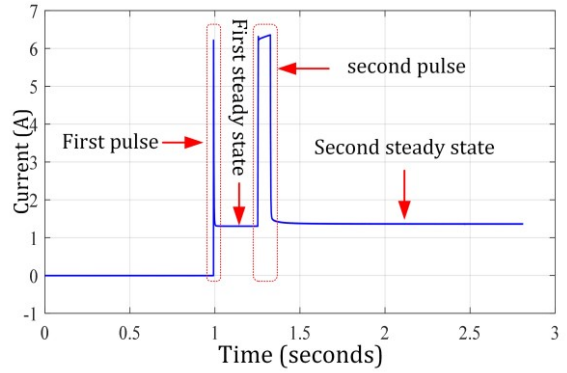

Figure 4: Response signal segmentation

In the response signal, the horizontal axis represents time, and the vertical axis represents the amplitude of the response current signal. The response signal contains two pulse signals, labelled as the "first pulse" and the "second pulse" respectively. Between the pulses, the signal reaches a steady state, defined as the "first steady state", and after the second pulse, it again reaches another steady state, defined as the "second steady state".

2.3.1 Adaptive Framing of the Response Signal Based on Pulse Matching

In order to extract geometric features from the response signal separately, adaptive framing of the response signal is required to identify the frames containing the first pulse and the second pulse. Once the first pulse and second pulse are determined, the segment between these pulses corresponds to the first steady state, and the segment following the second pulse corresponds to the second steady state. Considering the significant difference between the maximum and minimum values of the pulse signals, this section employs a sliding window drop method to match the pulses within the response signal and to perform adaptive framing accordingly.

Referring to the definition in Equation (2), assume similarly that the response signal is $\boldsymbol{S}_R$, the sampling rate is f_S, and the total signal length is n_R. Let the window width be w, with $w_2 \square n_R$. Overlapping windows are used to obtain the signal within each window of the response signal. Suppose the i-th frame is denoted as $\boldsymbol{F}_i$, where $\boldsymbol{F}_i$ represents a continuous segment of $\boldsymbol{S}_R$, starting from the i-th point in $\boldsymbol{S}_R$ and ending at the $(i+w_2-1)$-th point in $\boldsymbol{S}_R$.Under the overlapping window framing condition, the total number of frames n_2 in $\boldsymbol{S}_R$ is:

$$n_2 = n_R - w_2 + 1 \quad (8)$$

Assuming that in the i-th frame $\boldsymbol{F}_i$ obtained from the overlapping window, the maximum value is denoted as $F_{i,\max}$ and the minimum value is denoted as $F_{i,\min}$, then the drop $F_{i,PP}$ of this frame is defined as its peak-to-peak value:

$$F_{i,PP} = F_{i,\max} - F_{i,\min} \quad (9)$$

Under this condition, the peak-to-peak value sequence of the response signal $\boldsymbol{S}_R$ is denoted as $\boldsymbol{S}_{R,PP}$, with a length of n_2. Define the peak-to-peak threshold as Th_{PP}, and define the frame division line

sequence as $\boldsymbol{\alpha}$:

$$\boldsymbol{\alpha} = \begin{pmatrix} \alpha_1 & \alpha_2 & \cdots & \alpha_i & \cdots & \alpha_{n_2} \end{pmatrix} \tag{10}$$

Where α_i is determined by $F_{i,PP}$ and Th_{PP}:

$$\alpha_i = \begin{cases} 1, & F_{i,PP} \geq Th_{PP} \\ 0, & F_{i,PP} < Th_{PP} \end{cases} \tag{11}$$

Finally, based on the framing line sequence $\boldsymbol{\alpha}$, the response signal $\boldsymbol{S_R}$ is adaptively segmented. The elements in $\boldsymbol{\alpha}$ with a value of 1 are defined as valid framing lines, and the horizontal coordinates of these valid framing lines are denoted as: $t = \beta_i, i = 1, 2, \cdots$

2.3.2 Geometric Feature Extraction Based on Response Signal Framing

The geometric features defined and used in this study include: the number of frame division lines, the height of the first pulse, the RMS value of the first steady state, the transition time of the first steady state, the equivalent width of the second pulse, and the RMS value of the second steady state. Each geometric feature is introduced below, with a schematic diagram of the features shown in Figure 5.

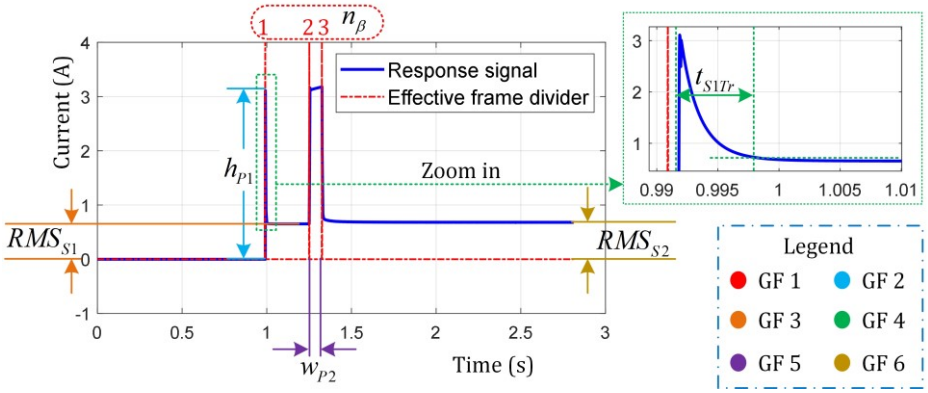

Figure 5: Geometric Feature Diagram

(1) Number of frame division lines

According to the definition of the adaptive frame division line sequence, the number of adaptive frame division lines n_β is:

$$n_\beta = \sum_{i=1}^{n_2} \alpha_i \tag{12}$$

(2) Height of the first pulse

According to the method of obtaining adaptive framing lines, the first pulse in the response signal $\boldsymbol{S_R}$ is located between $t \in [\beta_1, \beta_2)$. Therefore, the height of the first pulse h_{P1} is:

$$h_{P1} = \max\left(\boldsymbol{S_R}(t)\right), t \in \left[\beta_1, \beta_2\right) \tag{13}$$

(3) Effective value of the first steady state

Based on the definition of the adaptive framing lines, the first steady-state segment in the response signal $\boldsymbol{S_R}$ is located between $t \in \left[\beta_2 - \tau_1, \beta_2\right)$, where τ_1 is the time shift factor, and $\tau_1 < \beta_2 - \beta_1$. Therefore, the RMS value RMS_{S1} of the first steady state is:

$$RMS_{S1} = RMS\left(\boldsymbol{S_R}(t)\right), t \in \left[\beta_2 - \tau_1, \beta_2\right) \tag{14}$$

(4) First steady-state transition time

In control systems, transition time is defined as the shortest time taken for a controlled variable to return from its original steady state to a new equilibrium state after being subjected to a disturbance. In practical applications, it is typically defined as the shortest time taken for the controlled variable to enter and remain within ±5% of the new steady-state value. In the response signal, the first pulse is considered the disturbance, and the average value Sl of the first steady state $\overline{S1}$ is regarded as the steady-state value. Based on this, the time taken for the response signal to transition from the maximum value of P1 to $(1+5\%)\overline{S1}$ is defined as the first steady-state transition time t_{S1Tr}.

(5) Equivalent width of the second pulse

Under the condition that a second pulse exists in the response signal, the equivalent width w_{P2} of the second pulse is the time difference between the second adaptive segmentation line and the third effective segmentation line, i.e.:

$$w_{P2} = \beta_3 - \beta_2 \tag{15}$$

If due to a high-voltage load fault, the second pulse does not appear in the response signal, the width of the second pulse is defined as 0.

(6) Second steady-state effective value

Since the response signal gradually approaches a steady state after the high-voltage load system is closed, the longer the duration under load system closure, the more stable the response signal becomes. The effective value of the second steady state RMS_{S2} is defined as:

$$RMS_{S2} = RMS\left(\boldsymbol{S}_{\boldsymbol{R}}(t)\right), t \in \left[t_3 - \tau_2, t_3\right] \tag{16}$$

Where t_2 is defined in Equation (1), τ_2 is the time shift factor, and τ t_3.

2.3.3 Construction of Geometric Feature Vectors and Dictionary Matrix

Using the geometric features extracted from the aforementioned response signals, the geometric feature vector is constructed. The geometric feature vector $\boldsymbol{F}_{\boldsymbol{G}}$ contains six elements and is defined as:

$$\boldsymbol{F}_{\boldsymbol{G}} = \begin{pmatrix} n_\beta & h_{P1} & RMS_{S1} & t_{S1Tr} & w_{P2} & RMS_{S2} \end{pmatrix}^T \tag{17}$$

Assuming the i -th geometric feature vector sample under normal system operation is denoted as $\boldsymbol{F}_{\boldsymbol{G,NM,i}}$, the i -th geometric feature vector sample under battery heating film fault is denoted as $\boldsymbol{F}_{\boldsymbol{G,BHF,i}}$, the i -th geometric feature vector sample under DC-DC fault as $\boldsymbol{F}_{\boldsymbol{G,C,i}}$, and the i -th geometric feature vector sample under air-conditioning bus capacitor fault as $\boldsymbol{F}_{\boldsymbol{G,C,i}}$.

To classify load system faults using the sparse representation method, it is necessary to construct a dictionary matrix that includes geometric feature vector samples from all fault modes. Assuming the number of samples per mode in the dictionary matrix is q, the dictionary matrix composed of geometric feature vectors is:

$$\boldsymbol{D}_{\boldsymbol{G}} = \begin{pmatrix} \boldsymbol{D}_{\boldsymbol{G,NM}} & \boldsymbol{D}_{\boldsymbol{G,BHF}} & \boldsymbol{D}_{\boldsymbol{G,DCDC}} & \boldsymbol{D}_{\boldsymbol{G,C}} \end{pmatrix} \tag{18}$$

Where $\boldsymbol{D}_{\boldsymbol{G,NM}}$, $\boldsymbol{D}_{\boldsymbol{G,BHF}}$, $\boldsymbol{D}_{\boldsymbol{G,C}}$, and $\boldsymbol{D}_{\boldsymbol{G,DC}}$ are the submatrices composed of geometric feature vectors under normal mode, battery heating film fault, air-conditioning bus capacitor fault, and DC-DC fault conditions, respectively, and are defined as follows:

$$\boldsymbol{D}_{\boldsymbol{G,NM}} = \begin{pmatrix} \boldsymbol{F}_{\boldsymbol{G,NM,1}} & \boldsymbol{F}_{\boldsymbol{G,NM,2}} & \cdots & \boldsymbol{F}_{\boldsymbol{G,NM,i}} & \cdots & \boldsymbol{F}_{\boldsymbol{G,NM,q}} \end{pmatrix} \tag{19}$$

$$\boldsymbol{D}_{\boldsymbol{G,BHF}} = \begin{pmatrix} \boldsymbol{F}_{\boldsymbol{G,BHF,1}} & \boldsymbol{F}_{\boldsymbol{G,BHF,2}} & \cdots & \boldsymbol{F}_{\boldsymbol{G,BHF,i}} & \cdots & \boldsymbol{F}_{\boldsymbol{G,BHF,q}} \end{pmatrix} \tag{20}$$

$$\boldsymbol{D}_{\boldsymbol{G,DCDC}} = \begin{pmatrix} \boldsymbol{F}_{\boldsymbol{G,DCDC,1}} & \boldsymbol{F}_{\boldsymbol{G,DCDC,2}} & \cdots & \boldsymbol{F}_{\boldsymbol{G,DCDC,i}} & \cdots & \boldsymbol{F}_{\boldsymbol{G,DCDC,q}} \end{pmatrix} \tag{21}$$

$$\boldsymbol{D}_{\boldsymbol{G,C}} = \begin{pmatrix} \boldsymbol{F}_{\boldsymbol{G,C,1}} & \boldsymbol{F}_{\boldsymbol{G,C,2}} & \cdots & \boldsymbol{F}_{\boldsymbol{G,C,i}} & \cdots & \boldsymbol{F}_{\boldsymbol{G,C,q}} \end{pmatrix} \tag{22}$$

Based on the above definitions, the size of the dictionary matrix $\boldsymbol{D}_{\boldsymbol{G}}$, composed of geometric feature vectors, is $6 \times 4q$.

2.3.4 Sparse Representation Classification and Fault Diagnosis

The fault detection and diagnosis methods proposed in this research are mainly applied to the vehicle-mounted end. On the one hand, the computing capability of the onboard platform is limited, necessitating the minimisation of computational resource consumption during pattern recognition; on the other hand, to improve the accuracy of fault diagnosis, continuous expansion and replacement of samples in the dictionary matrix are required. Based on these demands, in order to enhance the efficiency and real-time performance of fault diagnosis and to strengthen the effectiveness of the dictionary matrix, this study employs a sparse representation method for pattern recognition and fault diagnosis, based on the extraction of signal geometric features.

The test samples are response signals obtained under the system offline state using the impulse signal described in equation (1). Assuming the acquired response signal is $\boldsymbol{S}_{\boldsymbol{R,Te}}$, geometric feature vectors are extracted from it using the signal framing method described above and denoted as $\boldsymbol{F}_{\boldsymbol{G,Te}}$. The sparse representation can then be expressed as:

$$\boldsymbol{F}_{\boldsymbol{G,Te}} = \boldsymbol{D}_{\boldsymbol{G}} \cdot \hat{\boldsymbol{r}} \tag{23}$$

Here, $\hat{\boldsymbol{r}}$ is the sparse vector whose number of elements corresponds to the number of samples in the dictionary matrix; the size of this vector is $4q \times 1$. Each element in the sparse vector represents the contribution of the labelled sample in the dictionary matrix to the representation of the test signal's feature vector. $\hat{\boldsymbol{r}}$ can be expressed as:

$$\hat{\boldsymbol{r}} = \begin{pmatrix} r_1 & \cdots & r_q & r_{q+1} & \cdots & r_{2q} & r_{2q+1} & \cdots & r_{3q} & r_{3q+1} & \cdots & r_{4q} \end{pmatrix}^T \tag{24}$$

After obtaining the sparse vector, for each mode, Set the obtained sparse vector to zero locally. The fault type of the test sample is determined based on the local vector with the minimum reconstruction error. For each mode, namely normal operation, battery heating film fault, DC-DC converter fault, and DC bus capacitor fault, the corresponding local sparse vector expressions are:

$$\hat{\boldsymbol{r}}_{\boldsymbol{NM}} = \begin{pmatrix} r_1 & \cdots & r_q & 0 & \cdots & 0 & 0 & \cdots & 0 & 0 & \cdots & 0 \end{pmatrix}^T \tag{25}$$

$$\hat{\boldsymbol{r}}_{\boldsymbol{EHF}} = \begin{pmatrix} 0 & \cdots & 0 & r_{q+1} & \cdots & r_{2q} & 0 & \cdots & 0 & 0 & \cdots & 0 \end{pmatrix}^T \tag{26}$$

$$\hat{\boldsymbol{r}}_{\boldsymbol{DCDC}} = \begin{pmatrix} 0 & \cdots & 0 & 0 & \cdots & 0 & r_{2q+1} & \cdots & r_{3q} & 0 & \cdots & 0 \end{pmatrix}^T \tag{27}$$

$$\hat{\boldsymbol{r}}_{\boldsymbol{C}} = \begin{pmatrix} 0 & \cdots & 0 & 0 & \cdots & 0 & 0 & \cdots & 0 & r_{3q+1} & \cdots & r_{4q} \end{pmatrix}^T \tag{28}$$

Based on each local sparse vector, the reconstruction error of the test sample is calculated respectively. The calculation method for the reconstruction error of the test sample is:

$$Err_i = \left\| \boldsymbol{F}_{G,Te} - \boldsymbol{D}_G \cdot \hat{\boldsymbol{r}}_i \right\|_2, \quad i = NM, EHF, DCDC, C \tag{29}$$

The index corresponding to the minimum value of Err_i is the mode of the test sample, i.e.:

$$Pattern = i, \quad s.t. \min\left(Err_i\right) \tag{30}$$

3. Case Analysis and Validation

3.1 Bench Design and Dataset Construction

To verify the effectiveness of the fault diagnosis method for high-voltage load systems proposed in this study, a test bench was constructed based on the high-voltage load system architecture of an electric heavy-duty truck, and typical faults were simulated. By injecting standard pulse excitation signals into the experimental system and synchronously collecting the circuit response current data, a dataset was established to validate and test the proposed algorithm. This study was conducted on a personal computer equipped with an AMD Ryzen 7 4800H with Radeon Graphics (2.90 GHz), 16 GB of RAM, and an NVIDIA GeForce GTX 1650 graphics card with 4 GB of video memory. The operating system was Windows 11, and the entire fault diagnosis process was carried out in the MATLAB R2023a environment.

The core components of the high-voltage load system test bench include the battery heating module,air conditioning DC bus capacitor, DC-DC converter, and their load circuits.

Since the power output from the DC-DC converter is primarily consumed through the DC motor load, the test bench is primarily equipped with the following functional load units: battery heating module, air conditioning bus capacitor, DC-DC converter, and a matched DC motor.

Additionally, a 21700-type lithium battery module is used to simulate an actual battery pack, providing a stable baseline power supply for the standard pulse excitation. The designed and developed test bench structure is shown in Figure 6, with a photograph of the test bench in Figure 7. The fault injection methods and sample abbreviations used to verify the proposed algorithm are listed in Table 1.

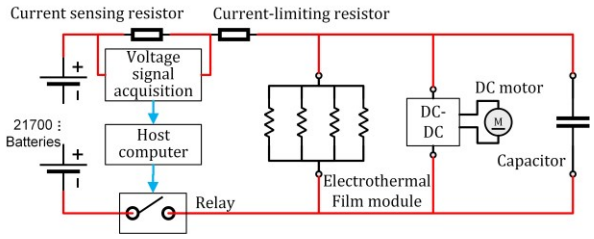

Figure 6: Structure of the experimental bench

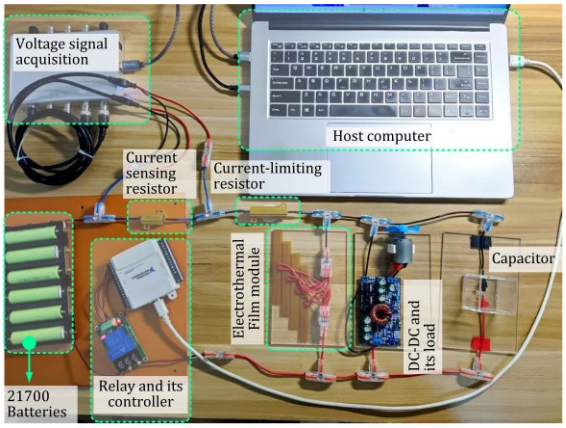

Figure 7: Fault detection and diagnosis test bench

In the experiment, according to the standard impulse signals $t_1 = 1$, $t_2 = 2$, $t_3 = 2.8125$ defined in equation (1), both the impulse signal u and the response signal $\boldsymbol{S}_R$ have a duration of $t_3 = 2.8125\text{s}$; the sampling rate is $f_S = 32000$, hence the total length of the response signal is $n_R = 90000$.

Table 1. Details of labelled samples and testing samples

Pattern	Details of fault injection	Abbreviation
Normal	-	NM
EHF fault: Partial short circuit	36.25% of single EHF short circuit	EHF_1
	46.72% of single EHF short circuit	EHF_2
	61.87% of single EHF short circuit	EHF_3
DC-DC fault: High-voltage coil connection fault	A 500-ohm resistor was connected in series with the 1st high-voltage coil	DCDC_1
	A 1000-ohm resistor was connected in series with the 1st high-voltage coil	DCDC_2
	The 1st high-voltage coil disconnection	DCDC_3
Capacitor fault: Capacitor degradation	11.82% capacitance degradation	C_1
	23.18% capacitance degradation	C_2
	33.18% capacitance degradation	C_3

3.2 Fault Detection Algorithm Verification

The fault detection algorithm proposed in this study relies solely on normal samples; therefore, the samples used to construct the healthy baseline include only response signal samples under normal conditions. To comprehensively verify the effectiveness of the fault detection algorithm across various modes, the test samples include response signals from both normal mode and various fault modes. The sample composition used in this section is shown in Table 2.

Table 2. Details of samples for fault detection validation

Type	Sample No. and details
Samples for health base construction	1st~60th: NM
Testing samples	1st~60th: NM
	61st~80th: EHF_1, 81st~100th: EHF_2, 101st~120th: EHF_3
	121st~140th: DCDC_1, 141st~160th: DCDC_2, 161st~180th: DCDC_3
	181st~200th: C_1, 201st~220th: C_2, 221st~240th: C_3

(1) Response signal framing and time domain feature extraction

When framing the response signal, the window width of the non-overlapping window adopted is $w_1 = 3000$, then the number of frames is $n_1 = 90000/3000 = 30$.

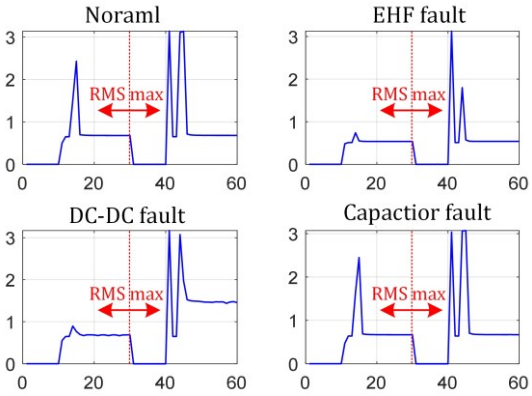

Figure 8: Time domain characteristic signal

Calculate the effective value and the maximum value of the response signal in each frame respectively to form the time-domain feature vector. The length of the time-domain feature vector $\boldsymbol{F}_T$ is $2n_1 = 60$.Taking the first sample of the four modes in Table 1 as an example respectively, their time-domain feature vectors are shown in Figure 8.

(2) Healthy baseline construction and calculation of Mahalanobis distance

Using the time-domain feature vectors extracted from the response signals of all normal mode samples, a healthy baseline is constructed. In this case, since the number of samples under the normal mode is $n_{Tr} = 60$, the size of the healthy baseline matrix $\boldsymbol{M}_{Tr}$ is $2n_1 \times n_{Tr} = 60 \times 60$, as shown in Figure 9. The horizontal axis represents the samples constituting the matrix, and the vertical axis represents the time-domain feature signals of each sample, composed of effective values and maximum values.

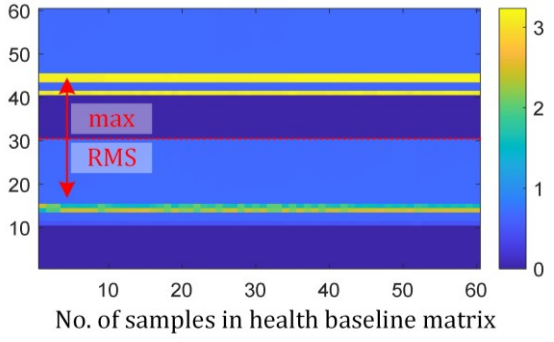

Figure 9: Healthy Baseline Matrix

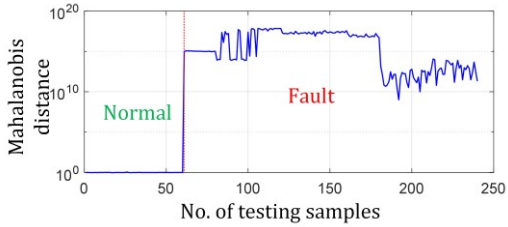

Figure 10: Marginal distance of test samples

Next, for all test samples listed in Table 2, time-domain feature vectors are extracted, and the Mahalanobis distance between each test sample's time-domain feature vector and the healthy baseline matrix is calculated. The Mahalanobis distances for all test samples are shown in Figure 10. As can be seen from the figure, the Mahalanobis distance effectively reflects the fault conditions of the test samples.

(3) Mahalanobis Distance Normalization and Fault Detection

To unify the scale of Mahalanobis distances obtained under various fault conditions, normalization is performed using equation (7), where the normalizing factor is $\alpha = 10$. According to the normalization principle, the fault detection indicators FDI for all test samples are shown in Figure 11. Here, the fault detection threshold is defined as $Th = 0.2$, meaning that when $FDI \geq 0.2$, the system is considered to be in a fault state; otherwise, the system is operating normally. From

Figure 11, it can be seen that the proposed fault detection algorithm effectively detects faults in all test samples.

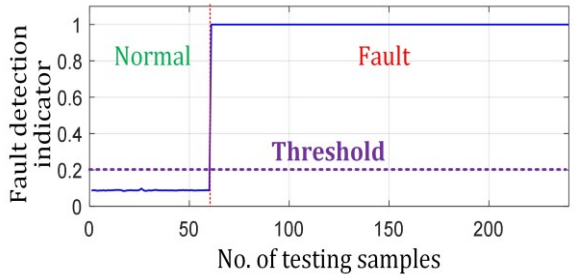

Figure 11: Test Sample Fault Detection Indicators

3.3 Validation of Fault Diagnosis Algorithm

To verify the effectiveness of the fault diagnosis algorithm proposed in this study, the response signal samples under each mode are divided into labeled samples and test samples. The labeled samples are used to extract geometric features and construct the dictionary matrix in the sparse representation framework. In contrast, the mode of the test samples is assumed to be unknown during testing, and their mode type is determined using the proposed algorithm. The identified results are then compared with the predefined true modes to calculate the fault diagnosis accuracy. The composition of labeled and test samples is shown in Table 3.

Table 3. Details of samples for fault diagnosis validation

Type	Pattern	No.	Sample details
Labelled samples	Normal	1^{st}~30^{th}	-
	Electrothermal film fault	31^{st}~60^{th}	31^{st}~50^{th}: EHF_1, 51^{st}~60^{th}: EHF_2
	DC-DC fault	61^{st}~90^{th}	61^{st}~80^{th}: DC-DC_1,81^{st}~90^{th}: DC-DC_2
	Capacitor upon AC fault	91^{st}~120^{th}	91^{st}~110^{th}: C_1,111^{st}~120^{th}: C_2
Testing samples	Normal	1^{st}~30^{th}	-
	Electrothermal film fault	31^{st}~60^{th}	31^{st}~40^{th}: EHF_2, 41^{st}~60^{th}: EHF_3
	DC-DC fault	61^{st}~90^{th}	61^{st}~70^{th}: DC-DC_2,71^{st}~90^{th}: DC-DC_3
	Capacitor upon AC fault	91^{st}~120^{th}	91^{st}~100^{th}: C_1,101^{st}~120^{th}: C_2

(1) Adaptive Framing of Response Signals Based on Pulse Matching

Based on the characteristics of the response signal, when framing the response signal in this section, the selected peak-to-peak threshold is $Th_{PP} = 0.2$. Based on this threshold, the effective framing lines for all labelled samples are obtained, as shown in Figure 12. In Figure, the horizontal axis represents the index of the labelled samples, while the vertical axis denotes the signal point index of the response signal. A value of 1 in the effective framing line corresponds to yellow dots in the figure, whereas all other values are 0, shown as the blue region.

A comparison of the effective framing lines under different modes in Figure 12 reveals that the number of effective framing lines differs significantly in the presence of battery heating film faults and DC-DC converter faults, compared to other modes.

Therefore, the number of effective framing lines can serve as one of the indicators for fault diagnosis.

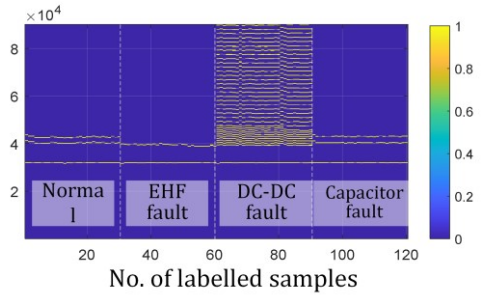

Figure 12: Effective Framing Lines

(2) Geometric feature extraction based on response signal framing

For all labelled samples, six geometric features were extracted based on the previously described method. The extraction methods for these geometric features are shown in Equations (12) to (16), with illustrative representations provided in Fig. 5. The extracted geometric features were normalised, and the geometric features of all labelled samples are presented in Fig. 13. A comparison of the geometric features of the labelled samples indicates that the six response signal geometric features proposed in this study can effectively distinguish between the different operating modes.

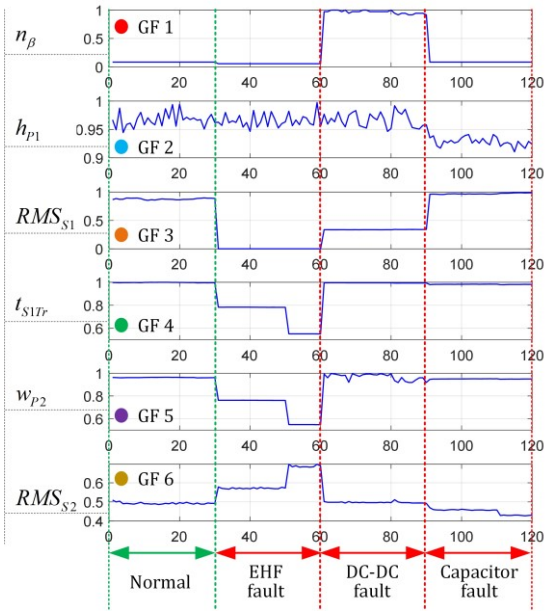

Figure 13: Geometric features of label samples

(3) Dictionary Matrix Construction, Sparse Expression Classification and Fault Diagnosis

The dictionary matrix is constructed based on the geometric features of all labelled samples. Since the number of labelled samples for each mode in the dictionary matrix is $q = 30$, the size of the dictionary matrix D is 6×120. A pseudo colour plot is used to visually represent the dictionary matrix, as shown in Figure 14. On this basis, according to Equation (23), the Batch Orthogonal Matching Pursuit method is employed to compute the sparse vectors for all test samples.

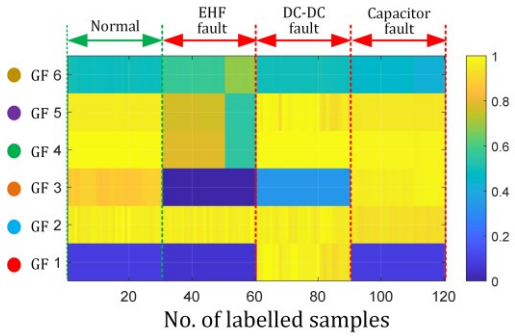

Figure 14: Geometric feature dictionary matrix

In the Orthogonal Matching Pursuit algorithm, the number of support vectors obtained per iteration is 2, with a total of 2 iterations. The sparse vectors and reconstruction errors for all test samples are shown in Figure 15. It can be seen that the values in the regions corresponding to the sparse vectors essentially reflect the fault types of the test samples. Through local zeroing and reconstruction error calculation, the mode of the test samples can be determined. In Figure 14, the modes of the test samples are indicated by red dots, demonstrating that all fault diagnosis results are consistent with the expected outcomes, thereby validating the effectiveness of the fault diagnosis method proposed in this study.

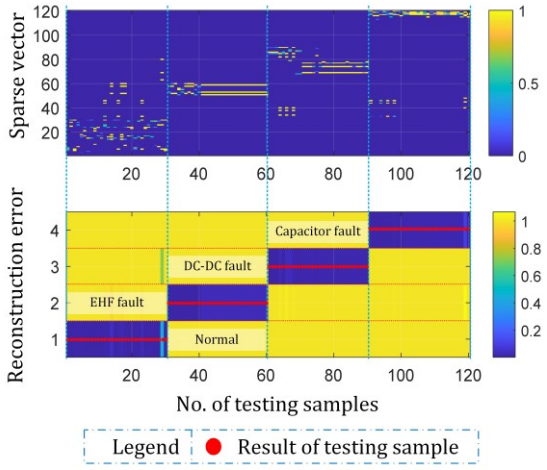

Figure 15: Sparse vectors and reconstruction error

(4) Robustness Evaluation under Noise

To further verify the generalisation capability of the proposed model under practical interference conditions, experiments were conducted by introducing Gaussian white noise at different signal-to-noise ratio (SNR) levels. As shown in Table 4, the model maintains stable detection accuracy across all noise levels. the model still achieves relatively high accuracy even under low SNR conditions, demonstrating its robustness in noisy environments.

Table 4. Performance comparison under different signal-to-noise ratio (SNR) levels

SNR levels	Inf	30	20	10	5	0
Diagnosis accuracy (%)	1.00	1.00	0.99	0.86	0.66	0.59
Detection accuracy (%)	1.00	1.00	1.00	1.00	1.00	1.00

3. Comparative Experiments

To verify the performance of the fault diagnosis scheme proposed in this study, it was compared with conventional fault diagnosis methods. In this section, Short-Time Fourier Transform (STFT) and Wavelet Packet Decomposition (WPD) were selected for feature extraction. Subsequently, classifiers

including deep learning networks (VGG16, AlexNet, ResNet), Support Vector Machine (SVM), K-Nearest Neighbors (KNN), Radial Basis Function (RBF), and Sparse Representation Classification (SRC) were employed to obtain fault diagnosis results, and compared with methods that use time-domain statistical features combined with classifiers such as SVM and RBF. The comparison of the results of different fault diagnosis methods is shown in Table 5 below.

Table 5. Comparison of results of different fault diagnosis methods

Diagnostic methods	**Diagnosis accuracy**	**Running time**
STFT+VGG16	100%	16s
STFT+AleNet	100%	14s
STFT+ResNet	98.33%	19s
WPD+SVM	74.17%	0.0748s
WPD+KNN	75.13%	0.0194s
WPD+RBF	75.83%	0.0130s
WPD+SRC	75%	0.0500s
Time domain statistical indicators + SVM	96%	0.0350
Time domain statistical indicators + RBF	92.5%	0.0120s
Fault diagnosis scheme proposed in this study	100%	0.3479s

As shown in Table 5, the signal geometric features extracted by the time-domain feature extraction method proposed in this study demonstrate stronger inter-class discriminability and better intra-class stability. In terms of real-time performance, the execution time of the main modules was recorded, and the average data processing time was 0.3479 seconds, which meets the requirement for rapid fault diagnosis.

To validate the effectiveness of the feature extraction approach presented herein, fault diagnosis was also performed based on wavelet packet decomposition and sparse representation. Except for the feature extraction algorithm, all other components remained consistent with the proposed scheme in this study, resulting in a diagnostic accuracy of 75%. Methods based on wavelet packet decomposition combined with Support Vector Machine (SVM), K-Nearest Neighbors (KNN), Radial Basis Function (RBF), and Sparse Representation Classification (SRC) exhibited shorter training times but relatively lower diagnostic accuracy.

By converting the raw signals into time-frequency maps via Short-Time Fourier Transform (STFT), subsequent neural network processing is facilitated. Approaches combining STFT with convolutional neural networks (VGG16, AlexNet, ResNet) achieved relatively high accuracy; however, their complex architectures resulted in longer running times, which is unfavourable for rapid diagnosis requirements. Fault diagnosis methods based on time-domain statistical features combined with classifiers such as SVM and RBF can generally meet diagnostic requirements; however, their performance is inferior to that of the method proposed in this study. Overall, considering both diagnostic accuracy and computational efficiency, the geometric feature extraction combined with sparse representation classification proposed in this paper presents significant advantages for fault diagnosis in EHT high-voltage load systems.

4. Conclusions

With the rapid advancement of new energy commercial vehicles towards high power and long endurance, the latent risk of faults in high-voltage electrical systems has significantly increased. Traditional multi-sensor fusion-based fault detection methods suffer from high deployment costs and poor adaptability to varying operating conditions, while existing single-signal diagnostic approaches largely rely on prior fault samples, making it difficult to meet the practical engineering demands of intelligent operation and maintenance for electric heavy truck. Addressing the engineering requirements for fault detection and diagnosis of high-voltage load systems in electric heavy truck, this paper proposes a system-level rapid diagnostic method based on impulse response signal analysis. Through theoretical derivation and experimental validation, the following conclusions are drawn:

The proposed fault detection method based on Mahalanobis distance requires only fault-free samples to establish the healthy baseline. The normalized fault detection indicator (FDI) effectively resolves the scale sensitivity issue inherent in conventional Mahalanobis distance methods, and its threshold criterion demonstrates strong robustness under complex operating conditions. The innovative pulse-matching framing algorithm achieves adaptive segmentation of response signals via a sliding window differential method, significantly improving geometric feature extraction efficiency compared to traditional fixed window-width techniques. The constructed six-dimensional geometric feature vector effectively distinguishes various fault types and modes, and when combined with sparse representation classification, enables accurate diagnosis of all test samples. The current signal used in this study is obtained from existing vehicle sensors and is acquired in real time by the vehicle's electronic control unit (ECU), with access provided via the CAN bus. The proposed method can serve as a supplementary module to the OBD-II diagnostic

framework, enabling the identification of signal anomalies that cannot be detected by conventional fault codes. In practical tests conducted on an in-vehicle computing platform, the proposed diagnostic method demonstrated low latency and minimal computational resource consumption per diagnostic cycle, thereby meeting the real-time requirements of onboard systems.

The main limitation of this study lies in the discrepancy between the experimental conditions and actual road scenarios. Future work will focus on developing more realistic fault models and implementing onboard deployment of the algorithm. By integrating with the vehicle bus through a standard CAN interface, the system will be able to process signals in real time and output diagnostic results. Additionally, the fault sample library will be expanded to enhance the capability of diagnosing compound faults. This study provides a novel technical approach for the condition monitoring of high-voltage systems in electric commercial vehicles and holds significant engineering value for improving vehicle safety.

References

[1] Sun Yan ming, Yang Yi le, & Li Qing li. (2023). Spatio-temporal Evolution Analysis of Carbon Emission Intensity of Provincial Transportation in China under the "Dual Carbon" Goals. Macroeconomic Research (11), 48-61.

[2] Zhang Lanyi, Weng Dawei, Wen Xiao juan, Zhang Huang fan, Hu Xisheng, Zeng Za qun. (2025) The path of energy conservation and carbon reduction in transportation under the background of green development transformation. Environmental science.

[3] He, H., Sun, F., Wang, Z., Lin, C., Zhang, C., Xiong, R., ... & Zhai, L. (2022). China's battery electric vehicles lead the world: achievements in technology system architecture and technological breakthroughs. *Green Energy and Intelligent Transportation*, 1(1), 100020.dol: https://doi.org/10.1016/j.geits.2022.100020

[4] Kumar, G. K., & Elangovan, D. (2020). Review on fault-diagnosis and fault-tolerance for DC–DC converters. IET Power Electronics, 13(1), 1-13. dol: https://doi.org/10.1049/iet-pel.2019.0672

[5] Wen, H., Li, J., Shi, H., Hu, Y., & Yang, Y. (2020). Fault diagnosis and tolerant control of dual-active-bridge converter with triple-phase shift control for bidirectional EV charging systems. IEEE Transactions on Transportation Electrification, 7(1), 287-303. dol: https://doi.org/10.1109/TTE.2020.3045673

[6] Zhou, N., He, H., Liu, Z., & Zhang, Z. (2017). UKF-based sensor fault diagnosis of PMSM drives in electric vehicles. Energy Procedia, 142, 2276-2283. Dol: https://doi.org/10.1016/j.egypro.2017.12.630

[7] Shi Ting na, Liu Bo, Yan Yan, & Xia Chang liang. (2025). Opportunities and Challenges of Industrial Application of Fault Diagnosis Technology for Motor Drive Systems. Proceedings of the CSEE.

[8] Mu Di, Wu Guo qi, Shao Lin, & You Shuai. (2021). Research on Control of Integrated Charging System for Small Busbar Capacitor Electric Vehicles. Power Electronics Technology, 55(09), 36-39.

[9] Jiang, Y., Yu, Y., & Peng, X. (2020). Online anomaly detection in DC/DC converters by statistical feature estimation using GPR and GA. *IEEE Transactions on Power Electronics*, 35(10), 10945-10957. Dol: https://doi.org/10.1109/TPEL.2020.2981500

[10] Lang, W, Hu, Y., Gong, C, Zhang, X., Xu, H., & Deng, J. (2021). Artificial intelligence-based technique for fault detection and diagnosis of EV motors: A review. IEEE Transactions on Transportation Electrification, 8(1), 384-406. dol: https://doi.org/10.1109/TTE.2021.3110318

[11] Zhang Chao, Du Bochao, Cui Shumei, Zheng Wei, & Han Shou liang. (2020). A capacitance value identification method for achieving quasi-online fault diagnosis of thin-film busbar capacitors in electric vehicles. Transactions of China Electrotechnical Society, 35(S1), 220-227. dol: https://doi.org/10.19595/j.cnki.1000-6753.tces.L80344

[12] Yu, Y., Zhao, Z., Chen, Y., Wu, H., Tang, C., & Gu, W. (2022). Evaluation of the applicability of IFRA for short circuit fault detection of stator windings in synchronous machines. IEEE Transactions on Instrumentation and Measurement, 71, 1-12. dol: https://doi.org/10.1109/TIM.2022.3201561

[13] Ashkezari, A. D., Ma, H., Saha, T. K., & Cui, Y. (2014). Investigation of feature selection techniques for improving efficiency of power transformer condition assessment. IEEE Transactions on Dielectrics and Electrical Insulation, 21(2), 836-844. dol: https://doi.org/10.1109/TDEI.2013.004090

[14] Zeinoddini-Meymand, H., & Vahidi, B. (2016). Health index calculation for power transformers using technical and economical parameters. IET Science, Measurement & Technology, 10(7), 823-830. dol: https://doi.org/10.1049/iet-smt.2016.0184

[15] Yu, H., Yu, Y., Wang, M., Xiong, W., Yuan, X., & Zou, X. (2021, May). A power transformer condition assessment method based on fuzzy nearness degree and improved cloud matter-element model. In *2021 IEEE 4th International Electrical and Energy Conference (CIEEC)* (pp. 1-6). IEEE. dol: https://doi.org/10.1109/CIEEC50170.2021.9510875

[16] Zeinoddini-Meymand, H., Kamel, S., & Khan, B. (2021). An efficient approach with application of

linear and nonlinear models for evaluation of power transformer health index. IEEE Access, 9, 150172-150186. dol: https://doi.org/10.1109/ACCESS.2021.3124845

[17] Zou Yang, He Jin, & Jin Tao. (2021). Evaluation Model of Transformer Oil-Paper Insulation State Based on NRS and DS Evidence Theory. Journal of Electric Machinery and Control, 25(10), 89-96. dol: https://doi.org/10.15938/j.emc.2021.10.010

[18] Tan, G., Liu, D., Shi, Y., & Yang, Z. (2020, September). Condition assessment method for power transformers based on variable weight principle and fuzzy comprehensive evaluation. In *2020 7th International Forum on Electrical Engineering and Automation (IFEEA)* (pp. 883-888). IEEE. dol: https://doi.org/10.1109/IFEEA51475.2020.00185

[19] You, X., Deng, Z., Yang, Y., Lin, X., & Hu, X. (2023). Fault diagnosis of electric city bus high-voltage load system based on multidomain sparse representation. *IEEE Transactions on Transportation Electrification*, 10(1), 1207-1221. dol: https://doi.org/10.1109/TTE.2023.3291053

[20] Arunachalam, K., Madanmohan, B., & Rajamani, R. (2020). Extended application for the impulse-based frequency response analysis: Preliminary diagnosis of partial discharges in transformer. *IEEE Access*, 8, 226897-226906. dol: https://doi.org/10.1109/ACCESS.2020.3045525

[21] Jeyabalan, V., & Usa, S. (2009). Frequency domain correlation technique for PD location in transformer winding. IEEE Transactions on Dielectrics and Electrical Insulation, 16(4), 1160-1167. dol: https://doi.org/10.1109/TDEI.2009.5211871

[22] Tian, A., Zhang, Y., Ma, C., Chen, H., Sheng, W., & Zhou, S. (2023). Noise-robust machinery fault diagnosis based on self-attention mechanism in wavelet domain. Measurement, 207, 112327.dol: https://doi.org/10.1109/TDEI.2009.5211871